

1 **Geomagnetic Conjugate Observations of Ionospheric Disturbances in**  
2 **response to North Korea Underground Nuclear Explosion on 3**  
3 **September 2017**

4  
5 Yi Liu, Chen Zhou\*, Qiong Tang, Guanyi Chen, and Zhengyu Zhao

6 Department of Space Physics, School of Electronic Information, Wuhan University,  
7 Wuhan, China

8

9 Corresponding to: [chenzhou@whu.edu.cn](mailto:chenzhou@whu.edu.cn)

10

11 **Key points:**

- 12 1. Geomagnetic conjugate ionospheric disturbances related to UNE were observed by  
13 IGS stations and Swarm satellite.
- 14 2. Radial propagation velocity from the UNE epicenter was calculated from temporal  
15 and spatial distribution of conjugate ionospheric disturbances.
- 16 3. The ionospheric disturbances present the evidence of the LAIC electric field  
17 penetration process.

18 **Abstract**

19 We report observations of ionospheric disturbances in response to North Korea  
20 underground nuclear explosion (UNE) on 3 September 2017. By using data from IGS  
21 (International GNSS Service) stations and Swarm satellite, geomagnetic conjugate  
22 ionospheric disturbances were observed. The observational evidences showed that  
23 UNE-generated ionospheric disturbances propagated radially from the UNE epicenter  
24 with the velocity of  $\sim 280$  m/s. We propose that the ionospheric disturbances are results  
25 of electrodynamic process caused by LAIC (Lithosphere-Atmosphere-Ionosphere  
26 Coupling) electric field penetration. LAIC electric field can also be mapped to the  
27 conjugate hemispheres along the magnetic field line and consequently cause  
28 ionospheric disturbances in conjugate regions. The UNE-generated LAIC electric field  
29 penetration plays an important role in the ionospheric disturbances in the region of the  
30 nuclear test site nearby and the corresponding geomagnetic conjugate points.

31

32 **Key words:** geomagnetic conjugate ionospheric disturbances; electrodynamic process;  
33 LAIC electric field penetration

## 34 **1 Introduction**

35 Ionospheric disturbances can be generated by various natural processes such as  
36 geomagnetic storms, internal electrodynamic instabilities and so forth. Furthermore,  
37 human activity can also cause evident ionospheric disturbances. Although underground  
38 nuclear explosion (UNE) is detonated deep in the lithosphere, ionospheric disturbances  
39 related to UNE can also be observed. By using GNSS-TEC observations, *Park et al.*  
40 (2011) reported that traveling ionospheric disturbances (TIDs) with phase velocity of  
41  $\sim 273$  m/s were generated by UNE in the 25 May 2009 North Korea UNE test. They  
42 proposed that acoustic gravity waves (AGWs) generated by the UNE can propagate to  
43 ionosphere and cause wavelike disturbances.

44  
45 While the observations of UNE related ionospheric disturbances have been discussed  
46 in (*Park et al.*, 2011; 2013), further investigation is still required to understand the  
47 mechanism(s) of ionospheric disturbance generation. Lithosphere-atmosphere-  
48 ionosphere coupling (LAIC) mechanisms originally proposed to interpret the linkage  
49 between ionospheric disturbances and earthquake activities are the most likely  
50 explanation for the ionospheric disturbances in response to UNE. The AGWs theory is  
51 one part of LAIC mechanisms (*Liu et al.*, 2016; *Maruyama et al.*, 2016). AGWs excited  
52 by the unusual events in lithosphere such as an earthquake or an UNE can propagate to  
53 ionospheric height and generate TID and electromagnetic disturbances (*Gokhberg et*  
54 *al.*, 1990; *Pokhotelov et al.*, 1994, 1995, 1999; *Mikhailov et al.*, 2000; *Huang et al.*,  
55 2011). However, the AGWs mechanism cannot fully explain all the observations related

56 to earthquakes. The electrostatic coupling is another candidate for LAIC mechanisms.  
57 During earthquakes, LAIC electric field or current can be excited by complex physical  
58 and chemical reactions induced by rock rupture and penetrate the ionosphere to promote  
59 plasma disturbances by  $E \times B$  motion (Xu *et al.*, 2011; Zhao & Hao, 2015). Zhou *et al.*  
60 (2017) developed an electric field penetration model for LAIC and their simulation  
61 results showed that the penetration height of LAIC electric field can reach to 400 km in  
62 mid-latitude regions. Because of high electric conductivity along the geomagnetic field  
63 lines, LAIC electric field can also be mapped along geomagnetic field lines and cause  
64 ionospheric disturbances at the geomagnetic conjugate points (Ruzhin *et al.*, 1998;  
65 Zhang *et al.*, 2009; Li & Parrot, 2017).

66

67 In this study, we have used magnetic conjugate GNSS observations and Swarm satellite  
68 to investigate the LAIC electric penetration effects of North Korea UNE on 3  
69 September 2017.

70

## 71 **2 Instrument and Data**

72 The IGS stations used in this study are located in East Asia and Australia. The  
73 geographical positions of the UNE and the IGS stations are showed in Figure 1. In order  
74 to eliminate the noise and multipath effects of GPS signals, only carrier phase  
75 observations are utilized to derive the relative slant total electron content (STEC). The  
76 time resolution is about 30 s. The ionospheric pierce points (IPPs) height in this study  
77 is assumed at 350 km. Figure 2 shows an example of time series of relative STEC

88 obtained by SUWN using satellite PRN 28 between 03:00-05:00 UT on 3 September  
 89 2017. To calculate the ionospheric disturbances related to UNE from GNSS  
 90 observations, the main trends of relative STEC strongly influenced by the Sun's diurnal  
 91 cycle need to be removed. In this study, the numerical third-order horizontal 3-point  
 92 derivatives of relative STEC are used for extracting the ionospheric disturbances (*Park*  
 93 *et al.*, 2011). In the first step, the numerical first-order horizontal 3-point derivatives  
 94 are taken as follows:

$$95 \quad \delta s_i = s_i - \frac{(s_{i-1} + s_{i+1})}{2} \quad i=\{2,\dots,n-1\} \quad (1)$$

96 where  $s_i$  is the  $i^{\text{th}}$  data point,  $\delta s_i$  is the first derivative, and n is the number of relative  
 97 STEC observations. The main relative STEC trends are removed through this process.  
 98 Figure 3(a) shows the time series of first-order derivatives of relative STEC. Waves  
 99 with small amplitudes occurred at around 3.9 and 4.1 hours, even though it was not  
 100 certain whether they were meaningful signals or just noises. The numerical derivative  
 101 formula is repeatedly performed on relative STEC derivatives to extract the ionospheric  
 102 disturbances related to UNE. The second-order derivatives can be written in the  
 103 following expression:

$$94 \quad \delta\delta s_i = \delta s_i - \frac{(\delta s_{i-1} + \delta s_{i+1})}{2} \quad i=\{2,\dots,m-1\} \quad (2)$$

95 where  $\delta\delta s_i$  is the second derivative, and m is the number of first derivative  
 96 observations. Figure 3(b) shows the time series of second-order derivatives of relative  
 97 STEC. Compared to the first-order derivatives presented in Figure 3(a), the amplitude  
 98 around the 3.9 hour was amplified while others were not significant. The third-order

99 derivatives are given as follows:

$$100 \quad \delta\delta\delta s_i = \delta\delta s_i - \frac{(\delta\delta s_{i-1} + \delta\delta s_{i+1})}{2} \quad i=\{2,\dots,l-1\} \quad (3)$$

101 where  $\delta\delta\delta s_i$  is the third derivative, and  $l$  is the number of second derivative  
 102 observations. Figure 3(c) shows the time series of third-order derivatives of relative  
 103 STEC. Compared to the second-order derivatives presented in Figure 3(b), the  
 104 disturbances around the 3.9 hour was further amplified. Therefore, compared to the  
 105 standard first derivatives, the numerical third-order horizontal  $l$ -point derivatives can  
 106 emphasized the more significant wave components with small amplitudes. Moreover,  
 107 to further remove the background noises of third-order derivatives of relative STEC,  
 108 the harr wavelet decomposition process is applied to the third-order derivatives.  
 109 Equations (4) and (5) give the harr wavelet function and scale function, respectively.

$$110 \quad \psi_H(t) = \begin{cases} 1 & 0 \leq t \leq 1/2 \\ -1 & 1/2 \leq t < 1 \\ 0 & \text{others} \end{cases} \quad (4)$$

$$111 \quad \phi_H(t) = \begin{cases} 1 & 0 \leq t < 1 \\ 0 & \text{others} \end{cases} \quad (5)$$

112 Figure 3(d) shows the wavelet de-noised third-order derivatives. From Figure 3(d), it  
 113 was found that the background noises in Figure 3(c) were completely removed and only  
 114 valuable wave components were retained.

115

116 Swarm mission operated by the European Space Agency (ESA) mainly focuses on the  
 117 survey of global geomagnetic field and its temporal evolution. Swarm mission consists  
 118 of three satellites named Alpha (A), Bravo (B), and Charlie (C). By using the magnetic

119 field data detected by Vector Field Magnetometer (VFM) on Swarm, the ionospheric  
120 radial current (IRC) density could be calculated by using spatial gradient of residual  
121 magnetic field data through Ampère's law (*Ritter et al.*, 2013). The field-aligned current  
122 (FAC) density could be also obtained by the ratio of the IRC density to the sine of the  
123 magnetic inclination angle. The FAC density and IRC density used in the study were  
124 provided by Swarm level 2 dataset with a time resolution of 1 s. The ionospheric current  
125 disturbances associated with UNE can also be calculated by the above method.

126

### 127 **3 Observations**

128 According to the measurements of China Earthquake Network Center (CENC), the  
129 approximate location of UNE on 3 September, 2017 is at 41.35 °N and 129.11 °E. The  
130 explosive time was at 03:30:01 UTC. The geomagnetic  $K_p$  index was less than 3 and  
131 AE index was less than 500 nT before and after the UNE, which indicates that the  
132 geomagnetic activity was not so active.

133

134 Figure 4 shows the time sequences of 3rd-order derivatives of carrier phase derived  
135 relative STEC by GNSS observations from different IGS stations in East Asia and  
136 Australia on 3 September 2017. All the GNSS observations from northern and southern  
137 hemisphere showed obvious short-period fluctuations within 2 hours after the UNE. It  
138 was also found that time delay after the UNE was different according to different IPPs  
139 of GPS signals. Figure 5 presents the IPPs tracks of relative STEC derivatives. In order  
140 to investigate the propagation velocity of ionospheric disturbances, we assumed that

141 the UNE-generated ionospheric disturbances propagate radially with a certain velocity.

142

143 Figure 6 illustrates the satellite Swarm B ionospheric current derivatives. Compared to

144 observed results of ionospheric current in quiet time, it was seen that the FAC

145 derivatives and IRC derivatives at conjugate hemispheres both showed obvious short-

146 period fluctuations after the UNE. The ionospheric current disturbances could reach 0.5

147  $\mu\text{A}\cdot\text{m}^{-2}\cdot\text{s}^{-3}$ .

148

149 Based on the UNE-IPPs horizontal distances and the ionospheric disturbances arrival

150 time, the horizontal propagation velocity of ionospheric disturbances could be

151 estimated by linear fitting model. The horizontal distance from IPPs to epicenter and

152 time delay of the UNE-generated ionospheric disturbances (STEC disturbances and

153 ionospheric current disturbances) are presented in Figure 7. Black triangle and green

154 triangle presented in Figure 7 represent the position of ionospheric current disturbances

155 in the northern hemisphere and the geomagnetic conjugate position of ionospheric

156 current disturbances in the southern hemisphere, respectively. The value of horizontal

157 velocity obtained by the least square estimation was  $\sim 280$  m/s.

158

## 159 **4 Discussion**

160 By utilizing geomagnetic conjugate GNSS TEC observations and ionospheric current

161 products from Swarm, we introduced the ionospheric disturbances which are

162 considered as a result of the UNE carried out by North Korea on 3 September 2017.



163 The method of the numerical third-order horizontal 3-point derivatives was applied to  
164 the GNSS TEC and the ionospheric current of Swarm to extract the ionospheric  
165 disturbances, which can also be found in *Park et al.*, (2011). Ionospheric disturbances  
166 derived from GNSS TEC observations in our study are consistent with the results of  
167 North Korea UNE on 25 May 2009 obtained by *Park et al.* (2011).

168

169 The effects of UNE on the ionosphere could be very similar to that of earthquakes on  
170 the ionosphere. In previous studies, AGWs are considered as the most likely mechanism  
171 for atmospheric and ionospheric disturbances excited by UNE or earthquakes  
172 (*Mikhailov et al.*, 2000; *Che et al.*, 2009; *Garrison et al.*, 2010; *Park et al.*, 2011, 2013;  
173 *Yang et al.*, 2012; *Maruyama et al.*, 2016). *Klimenko et al.* (2011) proposed that the  
174 ionospheric disturbances were generated by small-scale internal gravity waves (IGWs)  
175 through propagation and dissipation processes during seismic activity. *Liu et al.* (2016),  
176 and *Chum et al.* (2016, 2018) suggested that co-seismic ionospheric disturbances could  
177 be generated by long-period infrasound waves excited by seismic waves. However,  
178 AGWs mechanism cannot explain the geomagnetic conjugate observations in Figure 4,  
179 because mechanical waves such as AGWs cannot propagate to the other hemisphere.

180

181 Recent researches have shown that earthquake ionospheric disturbances could be  
182 attributed to not only the AGW mechanism but also the electrostatic coupling, which  
183 means the electric field or current penetration into ionosphere induced by earthquakes.  
184 Based on the observations of INTERCOSMOS-BULGARIA-1300 satellite and

185 DEMETER satellite, *Gousheva et al.* (2008, 2009) and *Zhang et al.* (2014) reported  
186 ionospheric quasi-static electric field perturbations during seismic activities. By using  
187 the magnetometer observations, *Hao et al.* (2013), and *Liu et al.* (2016) showed obvious  
188 ionospheric current and magnetic field perturbations after the Tohoku earthquake. They  
189 proposed that the seismo-traveling atmospheric disturbances (STADs) caused by  
190 infrasonic waves can propagate vertically into the ionosphere and modify the *E* layer  
191 Hall and Pedersen conductivity, resulting in background ionospheric electric field and  
192 magnetic field disturbances. *Pulinets et al.* (2000) proposed a quasi-electrostatic model  
193 for the LAIC mechanism. The simulation results indicated that the abnormal electric  
194 field induced by an earthquake can penetrate into the ionosphere to cause the  
195 ionospheric electric field disturbances (*Sorokin et al.*, 2001). The enhancement of TEC  
196 at the epicenter and its geomagnetic conjugate points were reported by *Liu et al.* (2011),  
197 which indicated that the earthquake-generated electric field penetration can be mapped  
198 along geomagnetic field lines to promote ionospheric disturbances at its conjugate  
199 points by electrodynamic process through  $\mathbf{E} \times \mathbf{B}$  drift. Therefore, the geomagnetic  
200 conjugation effects of ionospheric disturbances in Figure 4 can be explained by the  
201 UNE-generated electric field penetration. A schematic sketch of geomagnetic conjugate  
202 effect related to UNE in the region of the nuclear test site nearby and the corresponding  
203 geomagnetic conjugate region is shown in Figure 8. The UNE-generated electric field  
204 or current penetrates into the ionosphere and further generates an abnormal electric field  
205 at ionospheric altitude. The distribution of ionospheric electric field showed in Figure  
206 8 were calculated by LAIC electric field penetration model proposed by *Zhou et al.*

207 (2017). Because of the existence of high conductivity of geomagnetic field, the  
208 abnormal ionospheric electric field could be mapped along geomagnetic field lines.  
209 Geomagnetic conjugate ionospheric disturbances could be generated by abnormal  
210 ionospheric electric field through  $E \times B$  drift. Our study provides observational  
211 evidences of LAIC electric penetration other than acoustic gravity wave mechanism.

212

213 Geomagnetic conjugate observations in ionosphere have been reported by a few  
214 researchers. *Otsuka et al.* (2002; 2004) reported simultaneous observations of  
215 equatorial airglow depletions and medium-scale TIDs at geomagnetic conjugate points  
216 in both hemispheres by two all-sky imagers. Their results also suggested that  
217 polarization electric field, which is important for airglow depletion and MSTIDs  
218 generation, can be mapped along the field lines.

219

220 In our observations, we found that the ionospheric disturbances in both hemispheres  
221 caused by the UNE-generated electric field penetration propagated radially at the  
222 velocity of roughly 280 m/s in Figure 5 and Figure 7. LAIC electric field can be roughly  
223 estimated to be 14.5 mV/m, which is consistent with the magnitude of the earthquake-  
224 generated ionospheric electric field presented by *Zhang et al.* (2014). Figure 6 presents  
225 the results of the ionospheric current disturbances detected by the satellite Swarm B  
226 after the UNE. The reason may be that the ionospheric disturbances from the UNE  
227 propagate here to generate the current disturbances by electrodynamic process.

228

229 Moreover, compared with the magnitude and time scale of ionospheric disturbances  
230 caused by earthquakes, there are inconsistencies in our study. Based on IGS station  
231 observations around Tibet and Nepal, *Kong et al. (2018)* reported that TEC disturbances  
232 exceeded 0.3 TECU and lasted for 15-20 minutes during 2015 Nepal earthquake.  
233 However, it was found that the UNE-generated ionospheric disturbances were relatively  
234 smaller and lasted within 5 minutes in Figure 4. Therefore, it is possible to distinguish  
235 natural earthquakes and UNE events based on GNSS observations.

236

## 237 **5 Summary**

238 In this study, we have shown that the geomagnetic conjugate observations of GNSS  
239 TEC and ionospheric current from Swarm considered as a response to North Korea  
240 UNE on 3 September 2017. The LAIC electric penetration effects of UNE have been  
241 discussed in details. The main results are summarized as follows:

242

243 1. The ionospheric TEC and current disturbances were observed in both hemispheres  
244 after the UNE. According to the spatial-temporal relation, UNE-generated ionospheric  
245 disturbances propagated radially from the explosion epicenter with the velocity of ~  
246 280 m/s.

247

248 2. The ionospheric disturbances may be caused by LAIC electric penetration rather than  
249 AGWs. LAIC electric field induced by UNE penetrates into the ionosphere and causes  
250 plasma density disturbances near the nuclear test site and its conjugate points by

251 electrodynamic process.

252

253 **Acknowledgments**

254 We thank the use of GPS-TEC data from IGS Data Center of Wuhan University

255 (<http://www.igs.gnsswhu.cn/index.php/Home/DataProduct/igs.html>). We also

256 acknowledge the ESA for the Swarm data ([https://earth.esa.int/web/guest/swarm/data-](https://earth.esa.int/web/guest/swarm/data-access)

257 [access](https://earth.esa.int/web/guest/swarm/data-access)). The work is supported by the National Natural Science Foundation of China

258 (NSFC grant No. 41574146 and 41774162).

259 **References**

- 260 Che, I.-Y., Kim, T. S., Jeon, J.-S., and Lee, H.-I.: Infrasound observation of the apparent  
261 North Korean nuclear test of 25 May 2009, *Geophys. Res. Lett.*, 36, L22802, 2009.
- 262 Chum, J., Cabrera, M. A., Mořna, Z., Fagre, M., Baře, J., and Fiřer, J.: Nonlinear  
263 acoustic waves in the viscous thermosphere and ionosphere above earthquake, *J.*  
264 *Geophys. Res. Space Physics*, 121, 2016.
- 265 Chum, J., Liu, J.-Y., Podolsk K., and řindelrov, T.: Infrasound in the ionosphere  
266 from earthquakes and typhoons, *J. Atmos. Sol. Terr. Phys.*, 171, 72-82, 2018.
- 267 Garrison, J. L., Yang, Y.-M., and Lee, S.-C.: Observations of ionospheric disturbances  
268 coincident with North Korean underground nuclear tests, Abstract SA43B-1754  
269 presented at 2010 Fall Meeting, AGU, San Francisco, Calif., 13–17 Dec, 2010.
- 270 Gokhberg, M. B., Pilipenko, V. A., Pokhotelov, O. A., and Partasaraty, S.: Acoustic  
271 disturbance induced by underground nuclear explosion as source of electrostatic  
272 turbulence in the magnetosphere, *Doklady AN SSSR*, 313(N3), P568-574, 1990.
- 273 Gousheva, M., Danov, D., Hristov, P., and Matova, M.: Quasi-static electric fields  
274 phenomena in the ionosphere associated with pre- and post-earthquake effects, *Nat.*  
275 *Hazards Earth Syst. Sci.*, 8, 101-107, 2008.
- 276 Gousheva, M., Danov, D., Hristov, P., and Matova, M.: Ionospheric quasi-static electric  
277 field anomalies during seismic activity in August–September 1981, *Nat. Hazards*  
278 *Earth Syst. Sci.*, 9, 3-15, 2009.
- 279 Huang, Q.: Retrospective investigation of geophysical data possibly associated with the  
280 Ms8.0 Wenchuan earthquake in Sichuan, China, *J. Asian Earth Sci.*, 41(4-5): 421-

281 427, 2011.

282 Klimenko, M. V., Klimenko, V. V., Karpov, I. V., and Zakharenkova, I. E.: Simulation  
283 of Seismo-Ionospheric Effects Initiated by Internal Gravity Waves, *Russ. J. Phys.*  
284 *Chem. B*, 5(3), 393-401, 2011.

285 Kong, J., Yao, Y., Zhou, C., Liu, Y., Zhai, C., Wang, Z., and Liu, L.: Tridimensional  
286 reconstruction of the Co-Seismic Ionospheric Disturbance around the time of 2015  
287 Nepal earthquake, *J. Geodesy*, 3, 1-12, 2018.

288 Li, M., and Parrot, M.: Statistical analysis of the ionospheric ion density recorded by  
289 DEMETER in the epicenter areas of earthquakes as well as in their magnetically  
290 conjugate point area, *Adv. Space Res.*, 61(3), 974-984, 2017.

291 Liu, J. Y., Le, H., Chen, Y. I., Chen, C. H., Liu, L., Wan, W., Su, Y. Z., Sun, Y. Y., Lin,  
292 C. H., and Chen, M. Q.: Observations and simulations of seismo-ionospheric GPS  
293 total electron content anomalies before the 12 January 2010 M7 Haiti earthquake,  
294 *J. Geophys. Res.*, 116, A04302, 2011.

295 Liu, J. Y., Chen, C. H., Sun, Y. Y., Chen, C. H., Tsai, H. F., Yen, H. Y., Chum, J.,  
296 Lastovicka, J., Yang, Q. S., Chen, W. S., and Wen, S.: The vertical propagation of  
297 disturbances triggered by seismic waves of the 11 March 2011 M9.0 Tohoku  
298 earthquake over Taiwan, *Geophys. Res. Lett.*, 43(4), 1759-1765, 2016.

299 Maruyama, T., Yusupov, K., and Akchurin, A.: Ionosonde tracking of infrasound  
300 wavefronts in the thermosphere launched by seismic waves after the 2010 M8.8  
301 Chile earthquake, *J. Geophys. Res. Space Physics.*, 121, 2683-2692, 2016.

302 Mikhailov, Y. M., Mikhailova, G. A., and Kapustina, O. V.: VLF effects in the outer

303 ionosphere from the underground nuclear explosion on Novaya Zemlya island on  
304 24 October, 1990 (INTERCOSMOS 24 satellite data), *Phys. Chem. Earth Part C*,  
305 25(1–2), 93–96, 2000.

306 Otsuka, Y., Shiokawa, K., Ogawa, T., and Wilkinson, P.: Geomagnetic conjugate  
307 observations of equatorial airglow depletions, *Geophys. Res. Lett.*, 29, 1753, 2002.

308 Otsuka, Y., Shiokawa, K., Ogawa, T., and Wilkinson, P.: Geomagnetic conjugate  
309 observations of medium-scale traveling ionospheric disturbances at midlatitude  
310 using all-sky airglow imagers, *Geophys. Res. Lett.*, 31, L15803, 2004.

311 Park, J., Frese, R. R. B. von, Grejner-Brzezinska, D. A., Morton, Y., and Gaya-Pique,  
312 L. R.: Ionospheric detection of the 25 May 2009 North Korean underground  
313 nuclear test, *Geophys. Res. Lett.*, 38, L22802, 2011.

314 Park, J., Helmboldt, J., Grejner-Brzezinska, D. A., Frese, R. R. B. von, and Wilson, T.  
315 L.: Ionospheric observations of underground nuclear explosions (UNE) using GPS  
316 and the Very Large Array, *Radio Sci.*, 48, 463–469, 2013.

317 Pokhotelov, O. A., Pilipenko, V. A., Fedorov, E. N., Stenflo, L., and Shukla, P. K.:  
318 Induced electromagnetic turbulence in the ionosphere and the magnetosphere,  
319 *Physica Scripta*, 50, 600-605, 1994.

320 Pokhotelov, O. A., Parrot, M., Pilipenko, V. A., Fedorov, E. N., Surkov V. V., and  
321 Gladyshev V. A.: Response of the ionosphere to natural and man-made acoustic  
322 sources, *Ann. Geophys.*, 13, N11, 1197- 1210, 1995.

323 Pokhotelov, O. A., Pilipenko, V. A., and Parrot, M.: Strong atmospheric disturbances  
324 as a possible origin of inner zone particle diffusion, *Ann. Geophys.*, 17, 526-532,



325 1999.

326 Pulinet, S. A., Boyarchuk, K. A., Hegai, V. V., Kim, V. P., and Lomonosov, A. M.:  
327 Quasi-electrostatic model of atmosphere-thermosphere-ionosphere coupling, *Adv.*  
328 *Space Res.*, 26(8), 1209-1218, 2000.

329 Ritter, P., Lüth, H., and Rauberg, J.: Determining field-aligned currents with the Swarm  
330 constellation mission, *Earth Planets Space*, 65, 1285-1294, 2013.

331 Ruzhin, Y. Y., Larkina, V. I., and Depueva, A. K.: Earthquake precursors in  
332 magnetically conjugated ionosphere regions, *Adv. Space Res.*, 21(3), 525-528,  
333 1998.

334 Sorokin, V. M., Chmyrev, V. M., and Yaschenko, A. K.: Electrodynamic model of the  
335 lower atmosphere and the ionosphere coupling, *J. Atmos. Sol. Terr. Phys.*, 63(16),  
336 1681-1691, 2001.

337 Xu, T., Hu, Y., Wu, J., Wu, Z., Li, C., Xu, Z., and Suo, Y.: Anomalous enhancement of  
338 electric field derived from ionosonde data before the great Wenchuan earthquake,  
339 *Adv. Space Res.*, 47(6), 1001-1005, 2011.

340 Yang, Y.-M., Garrison, J. L., and Lee, S. C.: Ionospheric disturbances observed  
341 coincident with the 2006 and 2009 North Korean underground nuclear tests,  
342 *Geophys. Res. Lett.*, 39, L02103, 2012.

343 Zhao, B., and Hao, Y.: Ionospheric and geomagnetic disturbances caused by the 2008  
344 Wenchuan earthquake: A revisit, *J. Geophys. Res. Space Phys.*, 120, 5758–5777,  
345 2015.

346 Zhang, X., Shen, X., Liu, J., Ouyang, X., Qian, J., and Zhao, S.: Analysis of ionospheric

347 plasma perturbations before Wenchuan earthquake, *Nat. Hazards Earth Syst. Sci.*,  
348 9, 1259-1266, 2009.

349 Zhang, X., Shen, X., Zhao, S., Yao, L., Ouyang, X., and Qian, J.: The characteristics of  
350 quasistatic electric field perturbations observed by DEMETER satellite before  
351 large earthquakes, *J. Asian Earth Sci.*, 79(2), 42-52, 2014.

352 Zhou, C., Liu, Y., Zhao, S., Liu, J., Zhang, X., Huang, J., Shen, X., Ni, B., and Zhao,  
353 Z.: An electric field penetration model for seismo-ionospheric research, *Adv.*  
354 *Space Res.*, 60(10), 2217-2232, 2017.

355

356

357

358

359 **Figure Captions**

360 **Figure 1.** The positions of UNE and IGS stations. The position of 3 September 2017  
361 North Korea UNE is represented by black hollow start mark. The locations of IGS  
362 stations in both hemispheres are represented by red and blue squares, respectively.  
363 Lines of constant geomagnetic latitude are represented by black dashed lines.

364 **Figure 2.** An example of time series of relative STEC obtained by SUWN using  
365 satellite PRN 28 between 03:00-05:00 UT on 3 September 2017. The explosive time is  
366 represented by the red line.

367 **Figure 3.** The time sequences of derivatives of relative STEC obtained by SUWN  
368 station using satellite PRN 28 between 03:00-05:00 UT on 3 September 2017. (a) first-  
369 order derivatives, (2) second-order derivatives, (c) third-order derivatives, and (d)  
370 wavelet de-noised third-order derivatives. The explosive time is represented by the red  
371 line.

372 **Figure 4.** The time sequences of 3-order derivatives of carrier phase derived relative  
373 STEC by GNSS observations from different IGS stations in East Asia (left and middle  
374 column) and Australia (right column) on 3 September 2017. The blue lines indicate the  
375 wavelet de-noised 3-order derivative of relative STEC. The black lines indicate the GPS  
376 signal's elevation between the GNSS satellite and IGS stations. The explosive time is  
377 represented by the red line.

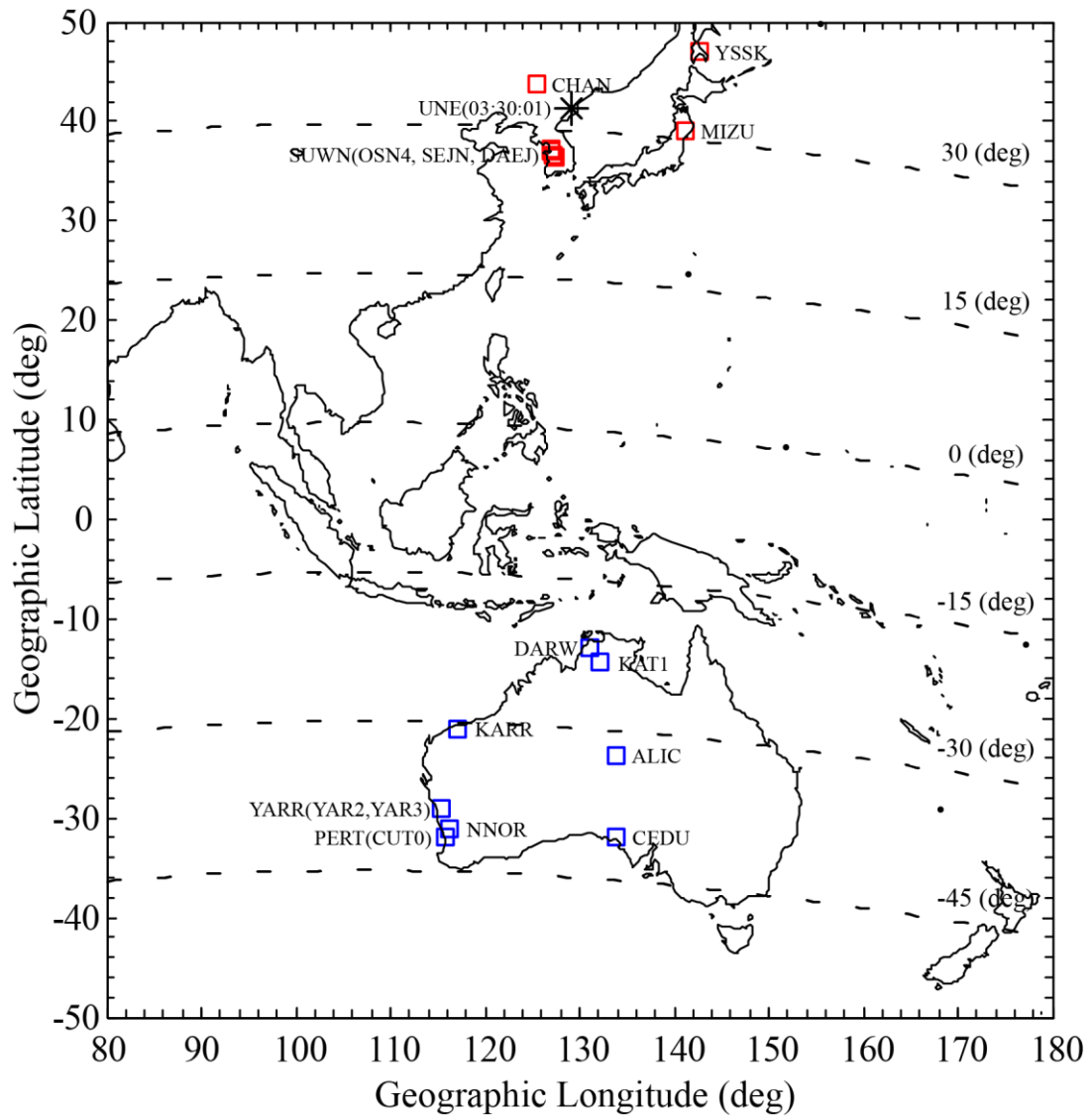
378 **Figure 5.** The IPPs tracks of relative STEC derivatives. The red lines indicate the IPPs  
379 tracks obtained by IGS stations in the northern hemisphere. The blue lines indicate the  
380 magnetic conjugate positions of the IPPs tracks obtained by IGS stations in the southern  
381 hemisphere. The positions of the maximum amplitudes of relative STEC derivatives in  
382 the northern hemisphere are represented by red triangles. The geomagnetic conjugate  
383 positions of the maximum amplitudes of relative STEC derivatives in the southern  
384 hemisphere are represented by blue triangles.

385 **Figure 6.** Results of Swarm B ionospheric current data analysis for the 2017 UNE: (a),  
386 (c), and (e) are the FAC, (b), (d), (f) are the IRC. From top to bottom, they indicate  
387 observations of Swarm B on 19 August 2017 (quiet time), 3 September 2017 (UNE

388 time), and 18 September 2017 (quiet time), respectively. The ionospheric current  
389 disturbances in response to UNE are represented by the red rectangles.

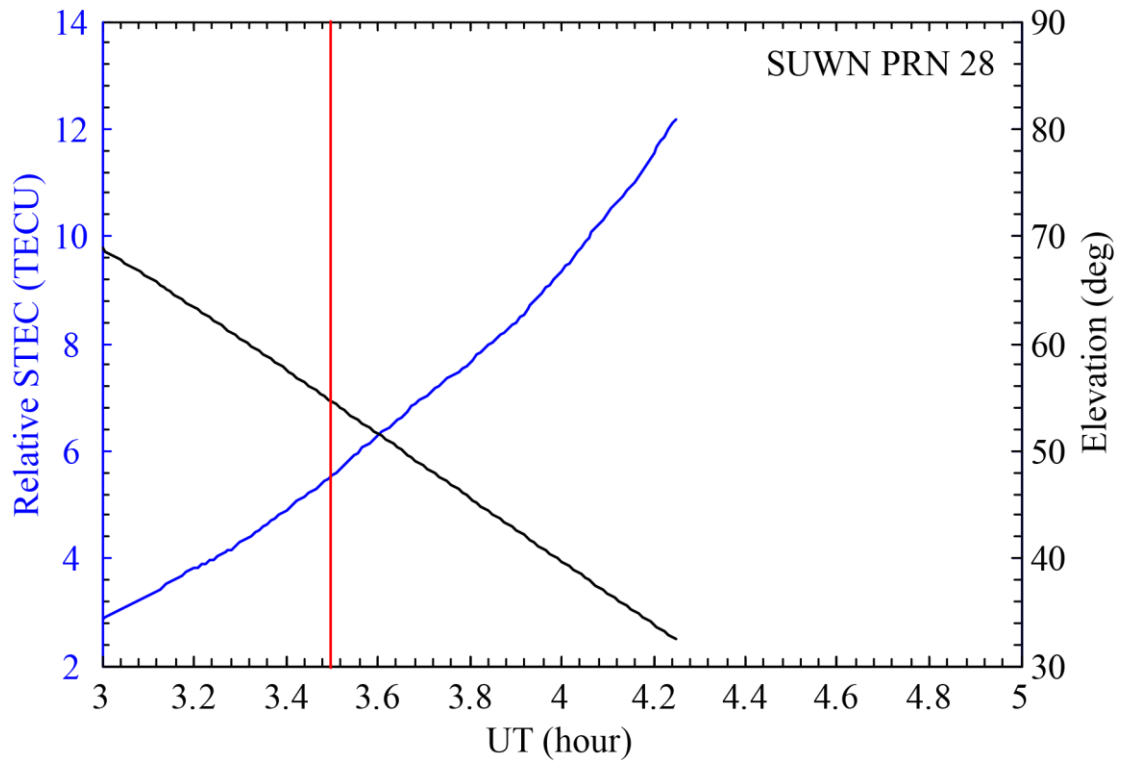
390 **Figure 7.** Horizontal distance-time data for the UNE-generated ionospheric  
391 disturbances. The black line indicates the fitting curve obtained by the least square  
392 method. The gray lines represent the boundaries of 95% confidence intervals. The red  
393 and blue triangles indicate same meanings as in Figure 5. The black triangle represents  
394 the position of ionospheric current disturbances in the northern hemisphere. The green  
395 triangle represents the geomagnetic conjugate position of ionospheric current  
396 disturbances in the southern hemisphere.

397 **Figure 8.** A sketch of geomagnetic conjugate effect related to UNE in the region of the  
398 nuclear test site nearby and the corresponding geomagnetic conjugate region.



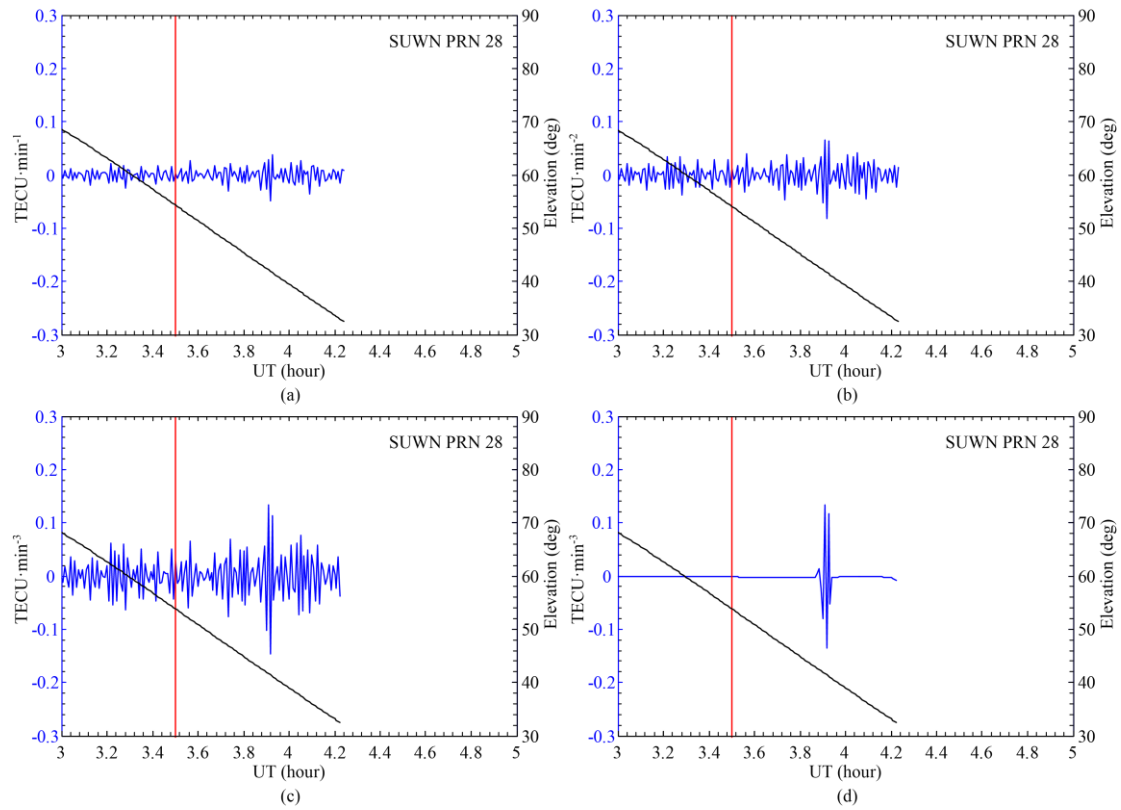
399  
 400  
 401  
 402  
 403  
 404  
 405  
 406

**Figure 1.** The positions of UNE and IGS stations. The position of 3 September 2017 North Korea UNE is represented by black hollow star mark. The locations of IGS stations in both hemisphere are represented by red and blue squares, respectively. Lines of constant geomagnetic latitude are represented by black dashed lines.



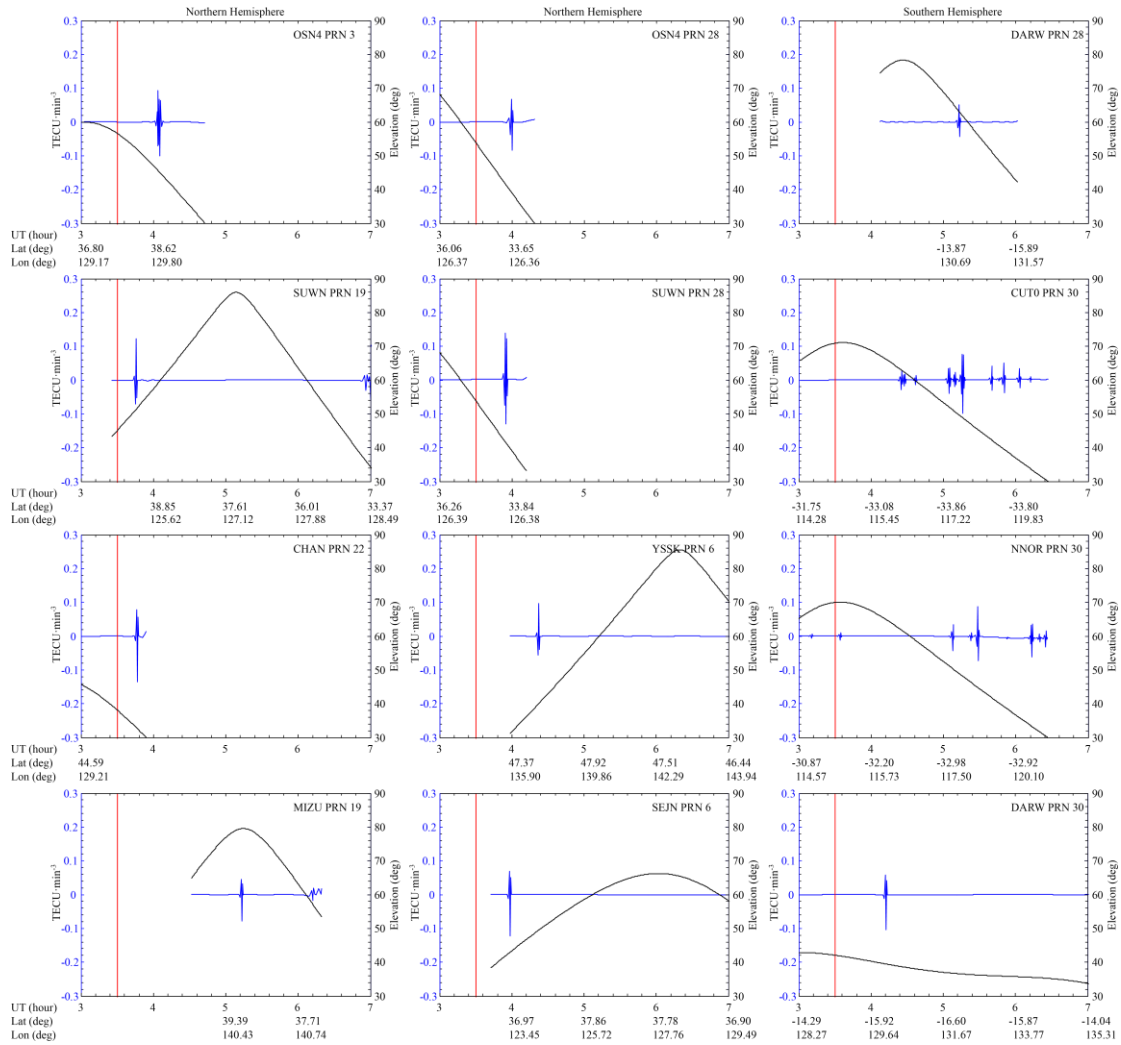
407

408 **Figure 2.** An example of time series of relative STEC obtained by SUWN using  
 409 satellite PRN 28 between 03:00-05:00 UT on 3 September 2017. The explosive time  
 410 is represented by the red line.



411

412 **Figure 3.** The time sequences of derivatives of relative STEC obtained by SUWN  
 413 station using satellite PRN 28 between 03:00-05:00 UT on 3 September 2017. (a)  
 414 first-order derivatives, (2) second-order derivatives, (c) third-order derivatives, and  
 415 (d) wavelet de-noised third-order derivatives. The explosive time is represented by the  
 416 red line.



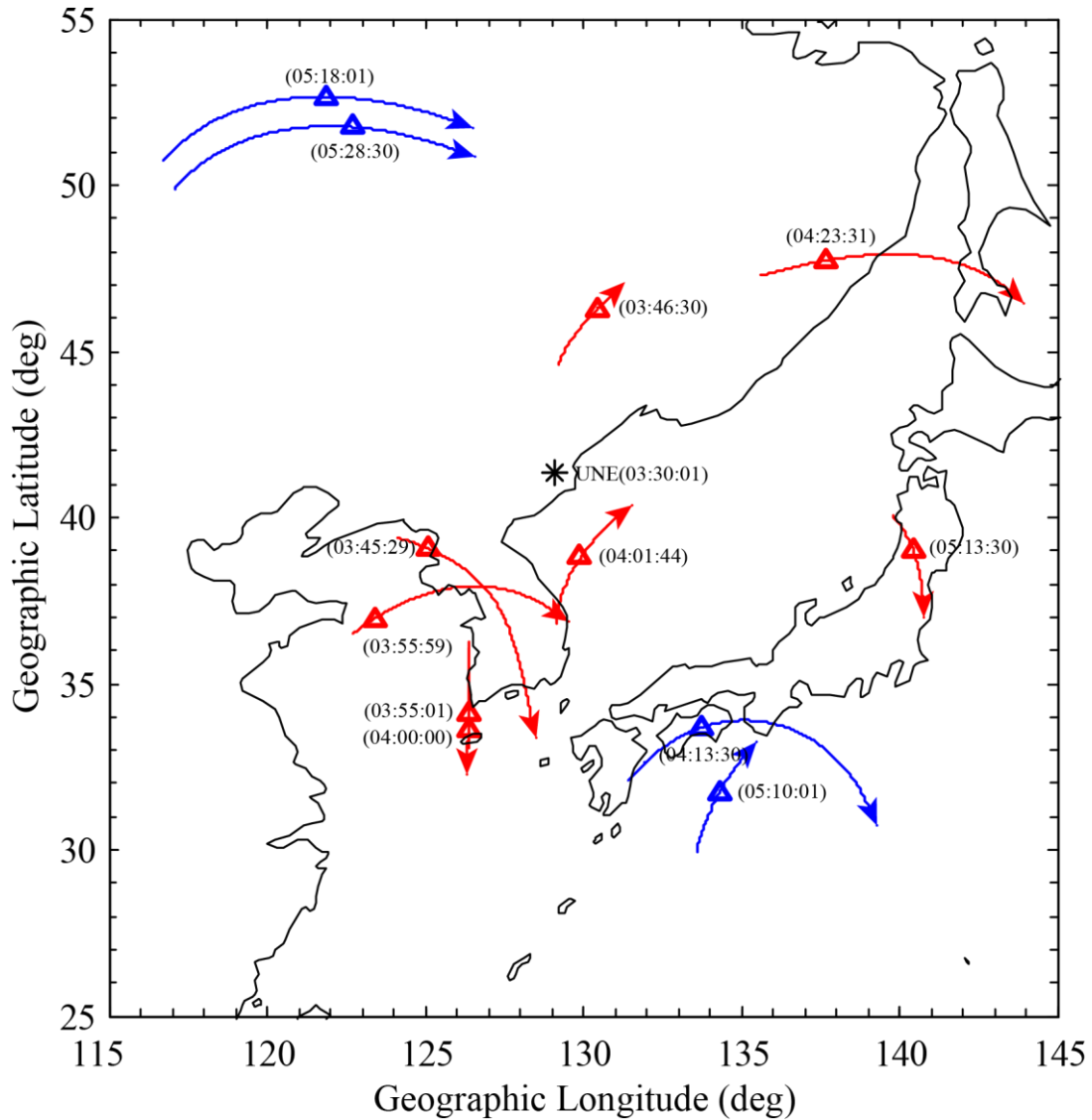
417

418

**Figure 4.** The time sequences of 3-order derivatives of carrier phase derived relative  
 419 STEC by GNSS observations from different IGS stations in East Asia (left and middle  
 420 column) and Australia (right column) on 3 September 2017. The blue lines indicate  
 421 the wavelet de-noised 3-order derivative of relative STEC. The black lines indicate  
 422 the GPS signal's elevation angle between the GNSS satellite and IGS stations. The  
 423 explosive time is represented by the red line.

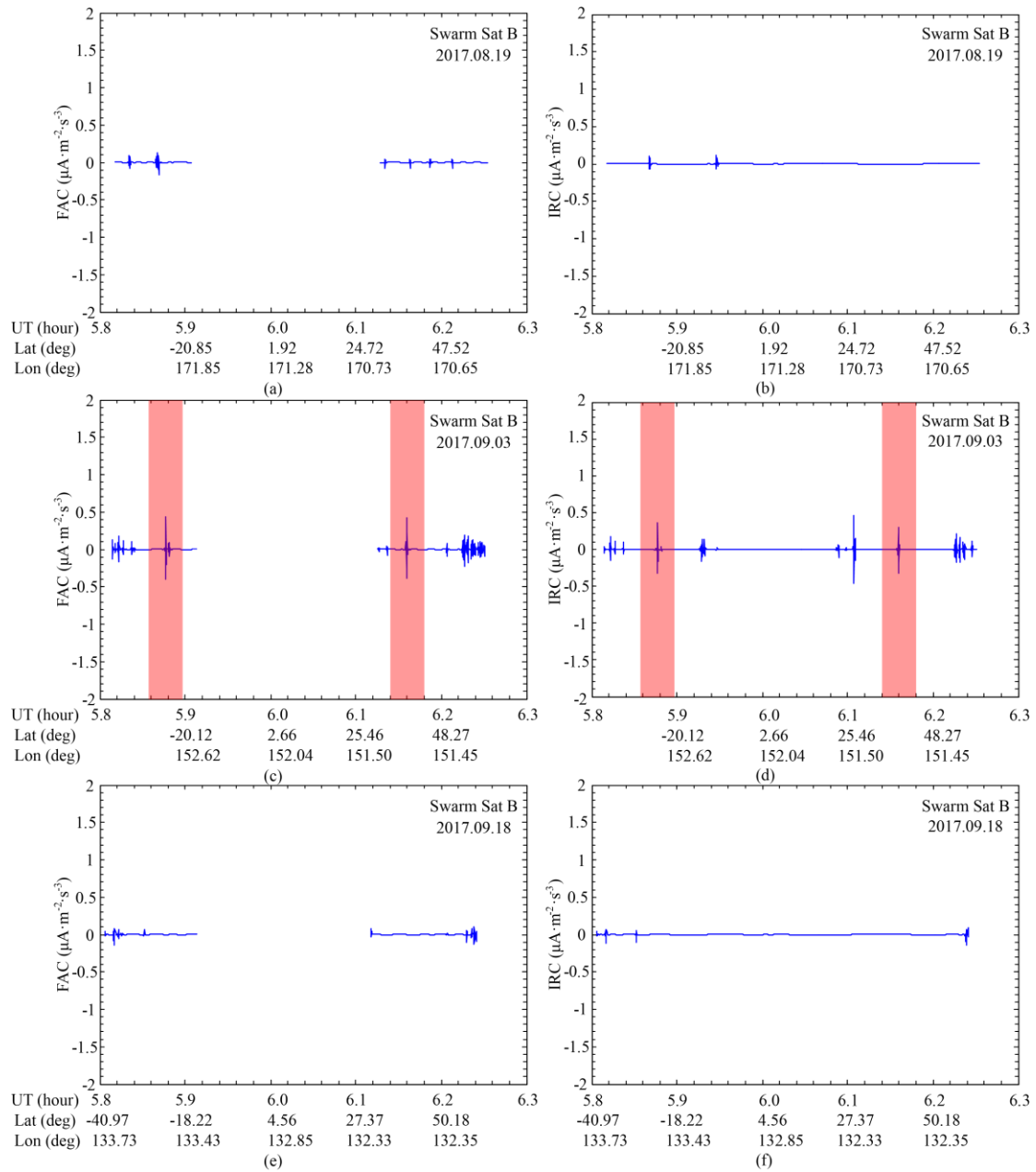
424





425

426 **Figure 5.** The IPPs tracks of relative STEC derivatives. The red lines indicate the  
 427 IPPs tracks obtained by IGS stations in the northern hemisphere. The blue lines  
 428 indicate the magnetic conjugate positions of the IPPs tracks obtained by IGS stations  
 429 in the southern hemisphere. The positions of the maximum amplitudes of relative  
 430 STEC derivatives in the northern hemisphere are represented by red triangles. The  
 431 geomagnetic conjugate positions of the maximum amplitudes of relative STEC  
 432 derivatives in the southern hemisphere are represented by blue triangles.



433

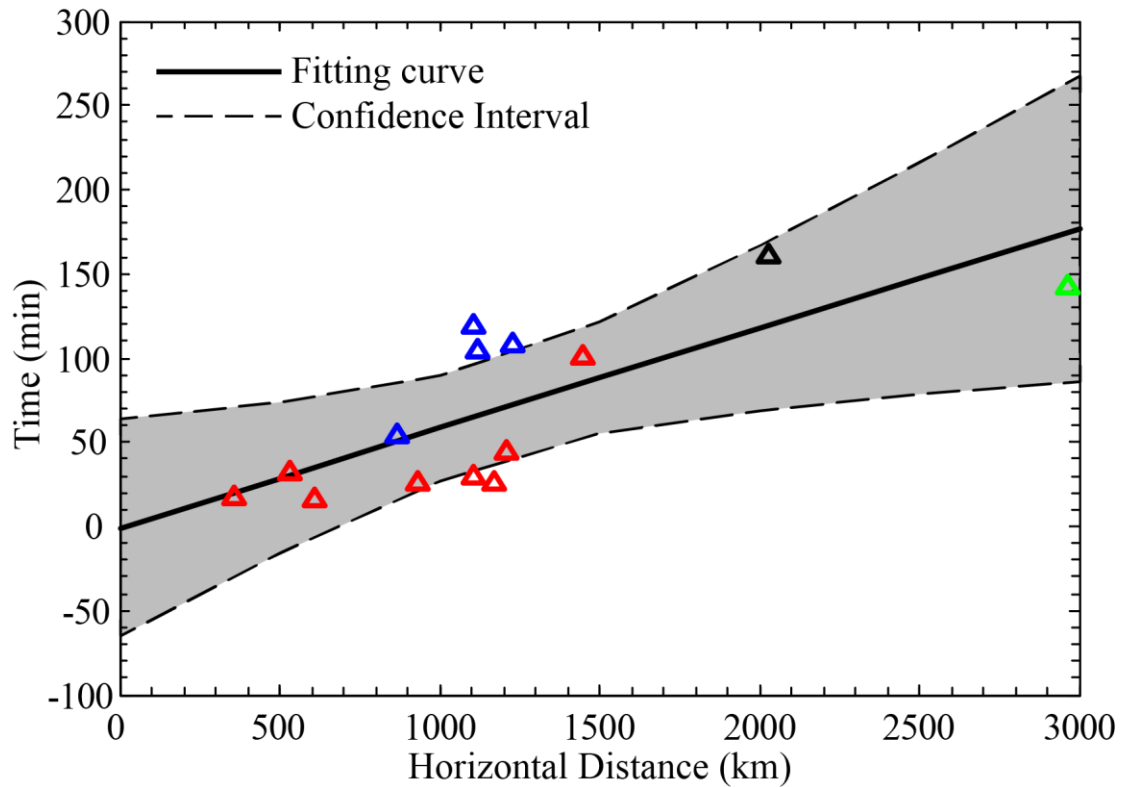
434 **Figure 6.** Results of Swarm B ionospheric current data analysis for the 2017 UNE:

435 (a), (c), and (e) are the FAC, (b), (d), (f) are the IRC. From top to bottom, they

436 indicate observations of Swarm B on 19 August 2017 (quiet time), 3 September 2017

437 (UNE time), and 18 September 2017 (quiet time), respectively. The ionospheric

438 current disturbances in response to UNE are represented by the red rectangles.



439

440

**Figure 7.** Horizontal distance-time data for the UNE-generated ionospheric disturbances. The black line indicates the fitting curve obtained by the least square method. The gray lines represent the boundaries of 95% confidence intervals. The red and blue triangles indicate same meanings as in Figure 5. The black triangle represents the position of ionospheric current disturbances in the northern hemisphere.

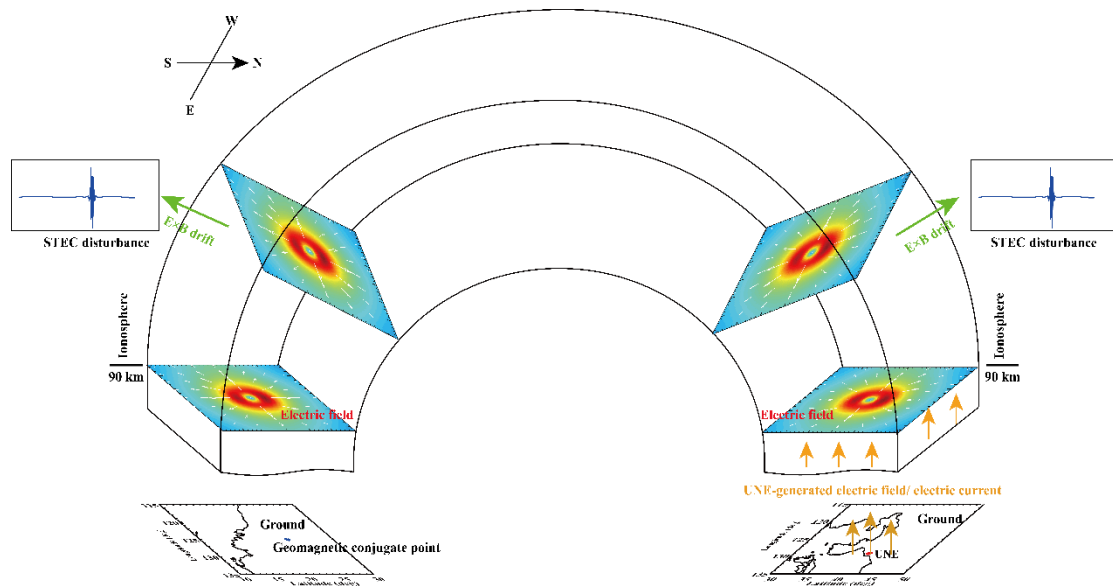
443

444

The green triangle represents the geomagnetic conjugate position of ionospheric current disturbances in the southern hemisphere.

446

447



448  
 449  
 450

**Figure 8.** A sketch of geomagnetic conjugate effect related to UNE in the region of the nuclear test site nearby and the corresponding geomagnetic conjugate region.